Nano Research

Open Access

Research Article

$Ir_xRu_{1-x}O_2/WO_3$ heterostructure for efficient acidic oxygen evolution reaction

Yi Tan[1,§], Yimin Li[1,§], Yuhao Wang[2,§], Xuyan Zhao[1], Deming Li[1], Song Gong[3] ✉, Yafei Li[2] ✉, Yu Zhang[1,4] ✉, and Yuen Wu[1,4] ✉

[1] *Department of Dermatology, the First Affiliated Hospital of the University of Science and Technology of China (USTC), Division of Life Sciences and Medicine, University of Science and Technology of China, Hefei 230001, China*
[2] *Jiangsu Key Laboratory of New Power Batteries, Jiangsu Collaborative Innovation Center of Biomedical Functional Materials, School of Chemistry and Materials Science, Nanjing Normal University, Nanjing 210023, China*
[3] *Department of Endocrinology, Tongji Hospital, Huazhong University of Science and Technology, Wuhan 430030, China*
[4] *Deep Space Exploration Laboratory, School of Chemistry and Materials Science, University of Science and Technology of China, Hefei 230026, China*
§ *Yi Tan, Yimin Li, and Yuhao Wang contributed equally to this work.*

Cite this article: *Nano Research*, **2026**, *19*, 94908622. https://doi.org/10.26599/NR.2026.94908622

ABSTRACT: Achieving simultaneous activity and durability for acidic oxygen evolution reaction (OER) remains a central challenge; interfacial heterostructuring offers a route to stabilize Ru while exploiting its high intrinsic activity. Here we report a heterostructured nanosheet catalyst $Ir_xRu_{1-x}O_2/WO_3$ that leverages interface-driven electronic and geometric modulation to boost OER performance. Density functional theory calculations indicate that interfacial modulation steers the OER toward the oxide pathway mechanism (OPM), effectively lowering the energy barrier of the potential-determining step. In electrochemical tests, the catalyst delivers an overpotential of 223 mV at 10 mA·cm^{-2} under acidic conditions and maintains an essentially constant potential over 120 h of continuous chronopotentiometry. An OER–oxygen reduction reaction (ORR) coupled electrochemical oxygen generator (EOG) single cell was constructed to evaluate the catalyst's performance, demonstrating a current density of 664 mA·cm^{-2} at 1.2 V and an oxygen production rate of 126 mL·min^{-1}. The $Ir_xRu_{1-x}O_2/WO_3$ exhibits good stability during 320 h of continuous operation, with a current decay of less than 3%, which is significantly lower than that of the commercial IrO_2 (current decay of ~ 15%). These results establish interfacial heterostructuring as a practical route to combine high activity with long-term durability in acidic OER, enabling efficient, robust electrochemical oxygen generation.

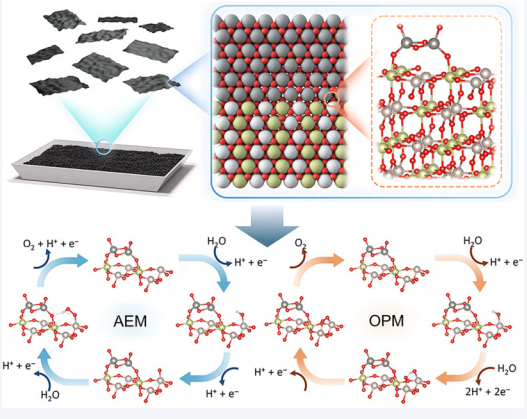

KEYWORDS: acidic oxygen evolution reaction, heterostructure, molten salt method, oxide pathway mechanism, electrochemical oxygen generator

1 Introduction

The acidic oxygen evolution reaction (OER) is essential to proton exchange membrane (PEM) based energy conversion systems [1–3]. Despite its central role, sluggish kinetics and oxidative corrosion at high potentials impose stringent demands on catalyst activity and durability. IrO_2 is widely regarded as the benchmark acidic-OER catalyst owing to its balanced overall performance [4–7]. Nevertheless, the scarcity and high cost of Ir severely restrict its large-scale deployment. In contrast, Ru-based catalysts offer a more cost-effective alternative and exhibit promising intrinsic OER activity in acidic media. Ru sites possess a moderate binding strength toward OER intermediates, which contributes to their high catalytic performance [8–10]. Yet, under harsh acidic and oxidative conditions, Ru tends to oxidize further into high-valent species, such as RuO_4, leading to rapid deactivation and metal dissolution [11, 12].

Received: January 27, 2026
Accepted: March 6, 2026

✉Address correspondence to Song Gong, gongsong@tjh.tjmu.edu.cn; Yafei Li, liyafei@njnu.edu.cn; Yu Zhang, zy11260@ustc.edu.cn; Yuen Wu, yuenwu@ustc.edu.cn

To address this issue, one effective strategy involves introducing Ir to stabilize the highly active Ru sites. When homogeneously dispersed at the atomic scale, IrRu bimetallic oxide ($IrRuO_x$) shows more favorable adsorption behavior toward OER intermediates [13–15]. Nevertheless, such alloying alone does not fundamentally resolve the intrinsic oxidative fragility of Ru, and the high cost of Ir further limits the industrial viability of this strategy [16]. To overcome the limitations of conventional bimetallic oxide, the construction of heterostructures has emerged as a particularly promising route to engineer the electronic structure at the atomic level [17–19]. The key lies in the spontaneous charge transfer across the interface, driven by differences in the intrinsic work functions of the constituent materials. This interfacial interaction redistributes the local electron density around the active sites [20]. According to the d-band center theory, such modulation of the electronic environment can effectively tailor the adsorption energies of key reaction intermediates [21–23]. By fine-tuning these interfacial effects, heterostructured catalysts not only preserve the high intrinsic activity of Ru but also achieve substantial improvements in operational durability.

In this study, we report a heterostructured nanosheet composed of $Ir_xRu_{1-x}O_2/WO_3$. By leveraging the interfacial interaction between WO_3 and the $Ir_xRu_{1-x}O_2$, the electronic structure of the active sites is effectively modulated, resulting in enhanced OER performance under acidic conditions. The catalyst exhibits a low overpotential of only 223 mV at a current density of 10 $mA{\cdot}cm^{-2}$ and maintains an essentially constant potential over 120 h of continuous chronopotentiometry measurement, outperforming the $Ir_xRu_{1-x}O_2$ reference sample. Density functional theory (DFT) calculations reveal that modulation of the active sites' structure and electronic density of states (DOS) via the WO_3 heterointerface enables $Ir_xRu_{1-x}O_2/WO_3$ to catalyze the OER through the oxide pathway mechanism (OPM), lowering the energy barrier. Then, the catalyst's application performance was validated by an OER–oxygen reduction reaction (ORR) coupled electrochemical oxygen generator (EOG) single cell. It revealed a remarkable current density of 664 $mA{\cdot}cm^{-2}$ at an operating voltage of 1.2 V, with an oxygen production rate of 126 $mL{\cdot}min^{-1}$ per single cell. Importantly, the $Ir_xRu_{1-x}O_2/WO_3$ costs only 55% as much as commercial IrO_2 while also exhibiting excellent operational durability: Over more than 320 h of continuous operation, its current decay rate is just 20% of that of commercial IrO_2. This work presents a promising strategy for designing high-performance acidic OER catalysts and highlights their potential in advanced electrochemical oxygen generation technologies.

2 Results and discussion

The $Ir_xRu_{1-x}O_2/WO_3$ heterostructured nanosheets were synthesized via a molten salt method. A precursor solution was mixed with sodium nitrate and subsequently annealed in air, yielding two-dimensional nanosheets composed of $Ir_xRu_{1-x}O_2$ and WO_3 crystalline grains (Fig. 1(a)). Scanning electron microscopy (SEM) and transmission electron microscopy (TEM) images reveal well-defined lateral dimensions and the characteristic two-dimensional morphology of the resulting nanosheets (Fig. S1 in the Electronic Supplementary Material (ESM)). Atomic force microscopy (AFM) further confirmed an ultrathin thickness of approximately 1.4 nm (Fig. 1(b)), consistent with a monolayer-like structure that facilitates the exposure of abundant active sites. For systematic comparative assessment, a suite of control materials—$Ir_xRu_{1-x}O_2$, IrO_2/WO_3, RuO_2/WO_3, IrO_2, and RuO_2—was synthesized using the same method. These samples exhibited similar nanosheet morphologies, as shown in Figs. S2 and S3 in the ESM.

High-angle annular dark-field scanning TEM (HAADF-STEM) image and elemental mapping images of $Ir_xRu_{1-x}O_2/WO_3$ reveal a uniform distribution of Ir, Ru, and W elements throughout the nanosheets (Fig. 1(c)). High-resolution TEM (HRTEM) image provides further insights into the crystalline arrangement of the nanosheets. The average grain size was estimated to be ~ 2.15 nm, indicating the formation of ultrasmall crystallites, which contribute to an increased surface area and a higher density of heterointerfaces (Fig. 1(d)). Detailed lattice fringe analysis revealed well-resolved interplanar spacings of 0.257 and 0.321 nm, corresponding to the (101) and (110) planes of $Ir_xRu_{1-x}O_2$, respectively, along with a 0.217 nm spacing attributed to the (222) plane of WO_3 (Figs. 1(e)–1(g)). These observations confirm the high crystallinity and distinct facet exposure of the $Ir_xRu_{1-x}O_2/WO_3$ heterostructure, validating the successful formation of the targeted hybrid architecture.

X-ray diffraction (XRD) measurements were first conducted to further verify the phase composition of the synthesized catalysts. The characteristic diffraction peaks of IrO_2, RuO_2, and WO_3 confirm the formation of $Ir_xRu_{1-x}O_2$ and WO_3 phases within the composite (Fig. 2(a) and Fig. S4 in the ESM). Raman spectroscopy was subsequently employed to investigate the structural features of the catalysts. In the RuO_2/WO_3, IrO_2/WO_3, and $Ir_xRu_{1-x}O_2/WO_3$ samples, the Raman bands located at approximately 257 and 795 cm^{-1} can be attributed to the bending (δ(W–O)) and stretching (ν(W–O)) vibrational modes of WO_3, respectively, indicating that the crystalline structure of WO_3 is preserved in the composites [24–26]. Additionally, peaks observed at around 525 and 643 cm^{-1} correspond to the symmetric stretching (E_g) of Ru–O or Ir–O bonds and asymmetric stretching (A_{1g}) vibrations of Ru–O bonds [27, 28]. In the $Ir_xRu_{1-x}O_2/WO_3$ sample, both the Ru–O/Ir–O and ν(W–O) modes exhibited varying degrees of blue shift, typically indicative of lattice distortion and oxygen vacancies induced by interfacial heterostructure effects (Fig. 2(b)) [29, 30].

The presence of oxygen vacancies was further probed using O 1s X-ray photoelectron spectroscopy (XPS) and electron paramagnetic resonance (EPR) spectroscopy. The O 1s XPS spectra display three major peaks at 530.0, 531.3, and 533.1 eV, corresponding to lattice oxygen (metal–oxygen bond (M–O)), oxygen vacancies, and adsorbed hydroxyl species, respectively (Fig. S5 in the ESM) [31]. Notably, the oxygen vacancy signal in $Ir_xRu_{1-x}O_2/WO_3$ exhibits a significantly larger peak area than in the control samples, with an area ratio of $O_{vacancy}$ to O_{M-O} reaching 4.11:1, suggesting a high concentration of oxygen vacancies in the heterostructure. This result was corroborated by EPR measurements, where $Ir_xRu_{1-x}O_2/WO_3$ showed a strong signal at g = 2.003, indicative of oxygen vacancies associated with lattice distortions (Fig. 2(c)) [32–34].

The evolution of metal element oxidation states was further examined by XPS measurement (Fig. S6 in the ESM). In the Ir 4f spectra, $Ir_xRu_{1-x}O_2/WO_3$ exhibits two main peaks at 62.5 and 65.5 eV, corresponding to the Ir $4f_{7/2}$ and Ir $4f_{5/2}$ components of Ir^{IV}, respectively (Fig. 2(d)). Compared to $Ir_xRu_{1-x}O_2$ (62.2 and 65.2 eV) and IrO_2/WO_3 (62.3 and 65.3 eV), these peaks display a slight positive shift, indicative of an increased oxidation state of Ir in the heterostructure [35]. While in the Ru $3p_{3/2}$ spectra, a dominant peak at 463.1 eV is consistently observed across all samples, corresponding to Ru^{IV} species, while a minor peak at 465.8 eV

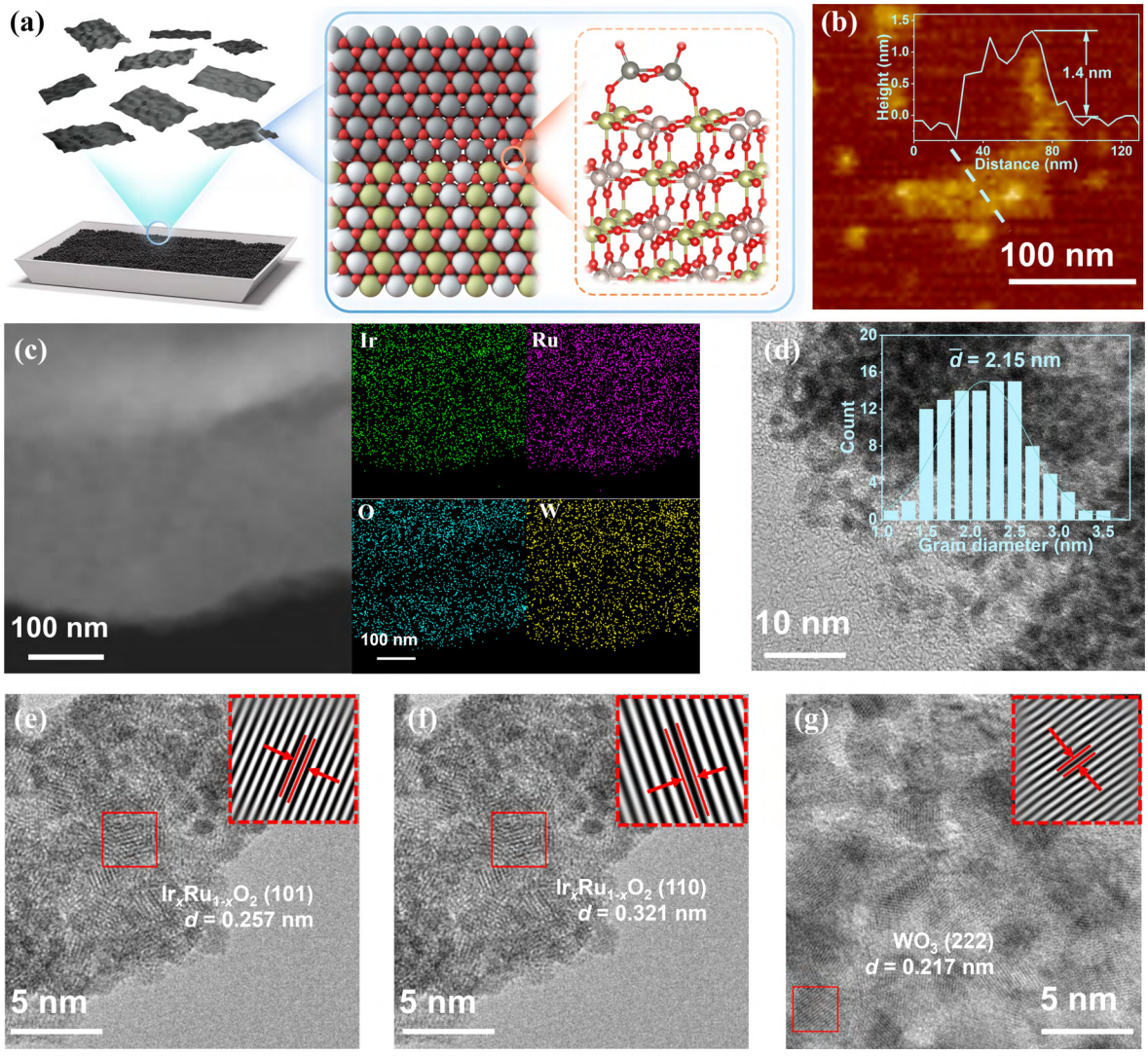

Figure 1 Schematic illustration of catalyst synthesis steps and morphological characterization. (a) Schematic illustration of the $Ir_xRu_{1-x}O_2/WO_3$ structure (green: Ir; light gray: Ru; dark gray: W; and red: O). (b) AFM image of $Ir_xRu_{1-x}O_2/WO_3$. (c) HAADF-STEM and corresponding elemental mapping images of $Ir_xRu_{1-x}O_2/WO_3$. (d) HRTEM image and grain size distribution analysis of $Ir_xRu_{1-x}O_2/WO_3$. ((e)–(g)) HRTEM and inverse fast Fourier transform (FFT)-HRTEM images of ((e) and (f)) $Ir_xRu_{1-x}O_2$ and (g) WO_3 grains in $Ir_xRu_{1-x}O_2/WO_3$.

reveals the presence of Ru^{III} species (Fig. 2(e)) [36]. The integrated area ratio of Ru^{III} to Ru^{IV} was calculated to evaluate the relative abundance of reduced species. $Ir_xRu_{1-x}O_2/WO_3$ exhibits the highest Ru^{III}/Ru^{IV} ratio (0.26), compared to $Ir_xRu_{1-x}O_2$ (0.23) and RuO_2/WO_3 (0.15), suggesting that both Ir and W incorporation promote the generation of Ru^{III} species. This partial reduction may contribute to enhanced stability by suppressing the overoxidation of Ru during the catalytic process. Additionally, the W 4f spectra reveal that the W^{VI} $4f_{7/2}$ and $4f_{5/2}$ peaks of $Ir_xRu_{1-x}O_2/WO_3$ appear at 34.9 and 37.0 eV, respectively (Fig. 2(f)), exhibiting a clear negative shift relative to those of IrO_2/WO_3 (35.4 and 37.5 eV) and RuO_2/WO_3 (35.5 and 37.6 eV) [37]. This downward shift indicates a partial reduction in W valence state, further confirming electronic structure reconstruction induced by the formation of the heterostructure.

The electrocatalytic performance of the synthesized samples was systematically evaluated using a standard three-electrode configuration. As shown in the linear sweep voltammetry (LSV) curves (Fig. 3(a)), $Ir_xRu_{1-x}O_2/WO_3$ exhibited the best OER activity in 0.5 M H_2SO_4 electrolyte, requiring an overpotential of only 223 mV to reach a current density of 10 mA·cm^{-2} (Fig. S7 in the ESM). This value is significantly lower than those of $Ir_xRu_{1-x}O_2$ (233 mV), IrO_2/WO_3 (278 mV), RuO_2/WO_3 (244 mV), IrO_2 (314 mV), and RuO_2 (305 mV). Moreover, $Ir_xRu_{1-x}O_2/WO_3$ exhibited a low Tafel slope of 53.1 mV·dec^{-1}, indicative of fast reaction kinetics (Fig. 3(b)).

In terms of mass activity, the $Ir_xRu_{1-x}O_2/WO_3$ catalyst showed a pronounced advantage due to its high intrinsic activity and reduced noble metal content, achieving 186 mA·mg$_{Ir,Ru}^{-1}$ at 1.45 V (vs. reversible hydrogen electrode (RHE)) and 537 mA·mg$_{Ir,Ru}^{-1}$ at 1.48 V (vs. RHE) (Fig. 3(c) and Fig. S8 in the ESM). Electrochemical impedance spectroscopy (EIS) was employed to probe the charge transfer properties at the electrode/electrolyte interface. The Nyquist plots (Fig. 3(d)) and the corresponding fitted values reveal that $Ir_xRu_{1-x}O_2/WO_3$ possesses the lowest charge transfer resistance (18.9 Ω), which is substantially lower than those of $Ir_xRu_{1-x}O_2$ (19.8 Ω), IrO_2/WO_3 (136.4 Ω), RuO_2/WO_3 (20.0 Ω), IrO_2 (560.0 Ω), and RuO_2 (349.3 Ω), suggesting more efficient interfacial electron transport (Table S2 in the ESM).

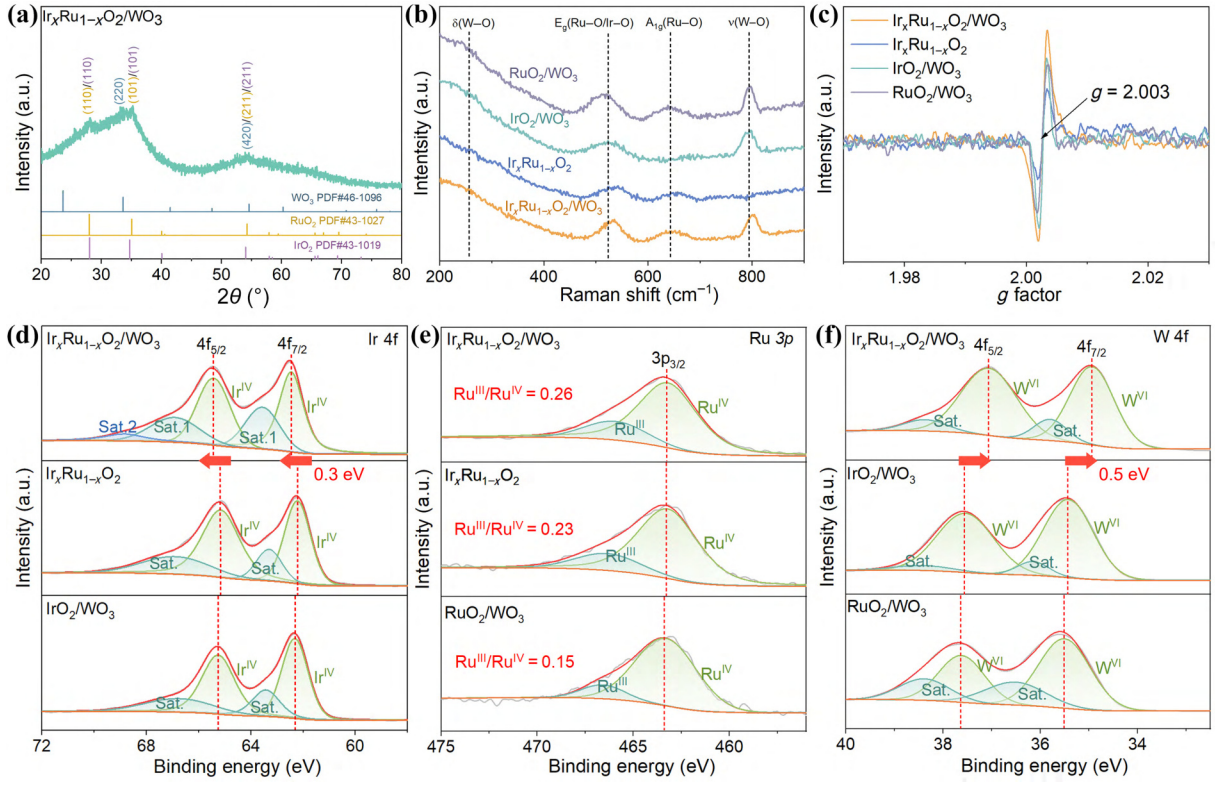

Figure 2 Structural characterization of the catalyst samples. (a) XRD patterns of catalyst samples. (b) Raman spectra of catalyst samples. (c) EPR spectra of catalyst samples. (d) Ir 4f, (e) Ru 3p, and (f) W 4f XPS spectra of catalyst samples.

The double-layer capacitance (C_{dl}) was measured from cyclic voltammetry (CV) in the non-Faradaic region to estimate the electrochemical surface area (ECSA) (Fig. 3(e) and Fig. S9 and Table S3 in the ESM). $Ir_xRu_{1-x}O_2/WO_3$ displayed the highest C_{dl} of 39.7 mF·cm^{-2}, significantly surpassing that of commercial IrO_2 (17.4 mF·cm^{-2}) and RuO_2 (3.4 mF·cm^{-2}), indicating a larger number of active sites afforded by its ultrathin nanosheet architecture.

To assess the OER stability of the $Ir_xRu_{1-x}O_2/WO_3$ catalyst, metal dissolution tests were performed at 10 mA·cm^{-2}. Although minor leaching of noble metals was observed at the initial stage, the dissolution gradually stabilized over time. After 30 h of continuous electrolysis, the cumulative dissolution ratios of Ru and Ir were only 6.0 wt.% and 0.9 wt.%, respectively (Fig. S10 in the ESM), demonstrating the catalyst's strong resistance to electrochemical degradation. To quantitatively evaluate the intrinsic durability, the stability number (S-number) was calculated based on the 30 h stability test (Fig. 3(f)). The $Ir_xRu_{1-x}O_2/WO_3$ catalyst achieved an S-number as high as 7.18×10^4, which outperforms those of $Ir_xRu_{1-x}O_2$ (4.06×10^4), IrO_2 (3.27×10^4), and RuO_2 (3.14×10^3). Considering that WO_3 may undergo dissolution under acidic conditions, we further quantified W leaching at 10 mA·cm^{-2}. After over 30 h of electrolysis, the cumulative W dissolution was 3.97 wt.%. Importantly, this extent of W loss did not cause any obvious performance degradation (Fig. S11(a) in the ESM). As evidenced by the LSV curves measured before and after the test, the overpotential at 10 mA·cm^{-2} increased by only 5 mV (from 228 to 233 mV) (Fig. S11(b) in the ESM). These results highlight the significant advantage of heterostructure engineering in enhancing the long-term stability of acidic OER catalysts. Furthermore, chronopotentiometry measurements revealed that $Ir_xRu_{1-x}O_2/WO_3$ maintained a nearly constant potential over 120 h of continuous operation (Fig. 3(g)), confirming its outstanding long-term electrochemical robustness. TEM images after stability test (Fig. S12 in the ESM) show that the overall morphology of the nanosheets remained well preserved, with no evidence of particle aggregation or structural collapse, thereby providing microscopic validation of the catalyst's structural stability throughout prolonged electrochemical cycling. Meanwhile, comparison with other previously reported Ir- and Ru-based catalysts shows that this catalyst exhibits both a relatively low Tafel slope and a low overpotential (Fig. 3(h)), demonstrating favorable OER activity in acidic media.

To evaluate the compositional robustness and scalability of the $Ir_xRu_{1-x}O_2/WO_3$ catalyst, a series of samples with varying Ir:Ru:W precursor ratios was synthesized. The morphology and crystal structure of these samples were characterized by TEM, SEM, and XRD, confirming that the variation in precursor ratios did not induce any significant structural differences (Figs. S13 and S14 in the ESM). Subsequently, all synthesized samples were evaluated for OER performance in 0.5 M H_2SO_4, with overpotentials ranging narrowly between 223 and 228 mV and Tafel slopes spanning 50.4–53.1 mV·dec^{-1} (Fig. S15 in the ESM). This indicates a high degree of compositional tolerance within the catalytic system, suggesting that the electrocatalytic performance is largely insensitive to moderate fluctuations in precursor ratios. Such low sensitivity is particularly valuable for practical large-scale synthesis, as it enhances process reliability and improves product yield. Building on this, the initial precursor quantity was further scaled up by 20-fold to evaluate the adaptability and consistency of the synthetic strategy under large-scale conditions. The appearance and morphology of the resulting large-scale sample are shown in Figs. S16 and S17 in the ESM. Electrochemical measurements revealed

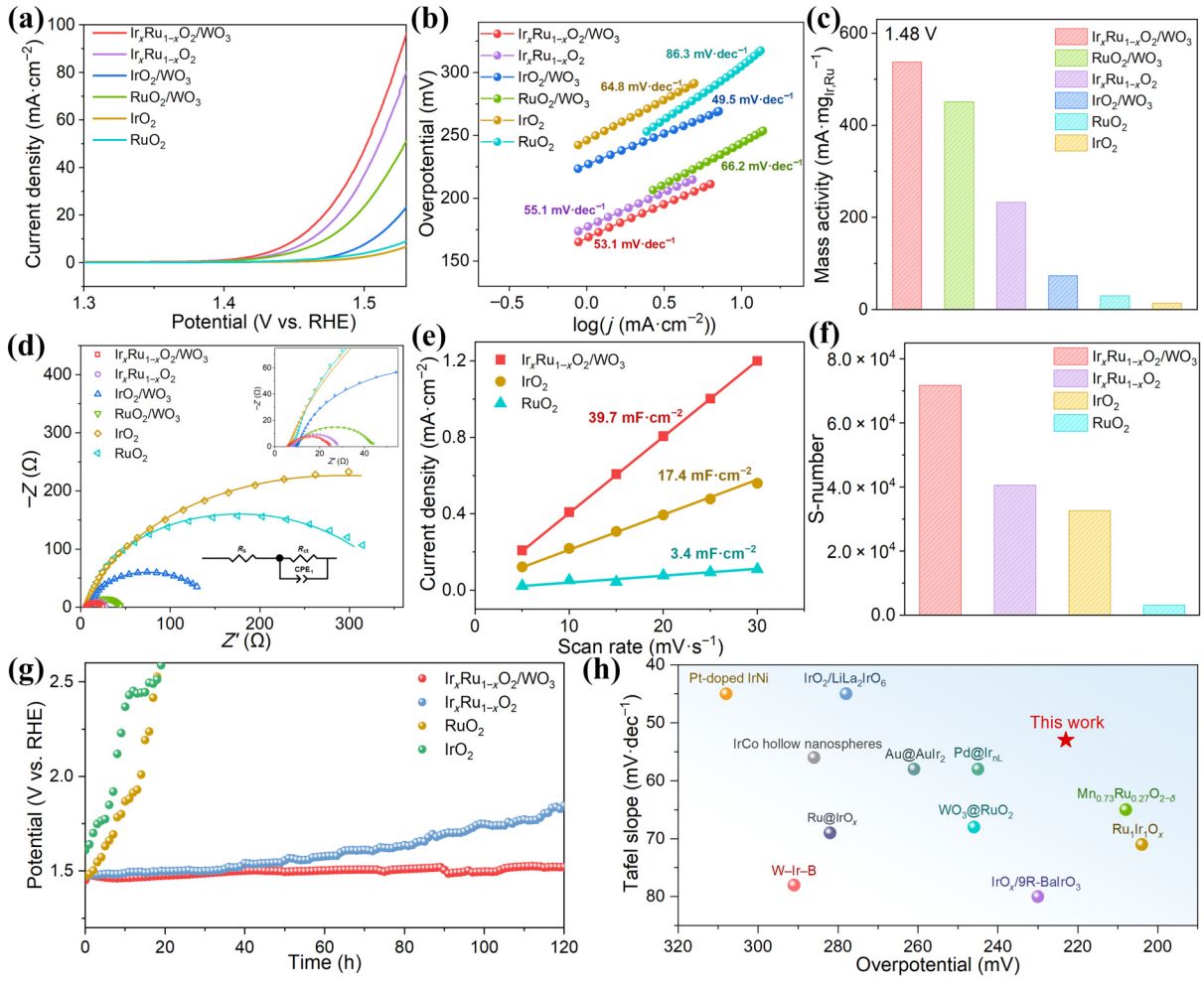

Figure 3 Electrocatalytic OER performance evaluation of the catalyst samples in acidic media. (a) LSV curves of catalyst samples in 0.5 M H_2SO_4. (b) Tafel plots of catalyst samples. (c) Corresponding mass activities of catalyst samples at 1.48 V (vs. RHE). (d) Nyquist plots and equivalent circuit diagram of catalyst samples at the applied potential of 1.47 V (vs. RHE). (e) C_{dl} plots of catalyst samples derived from CV curves at different scan rates from 5 to 30 mV·s^{-1}. (f) S-number of catalyst samples after 30 h chronopotentiometry tests at 10 mA·cm^{-2}. (g) Chronopotentiometry tests at 10 mA·cm^{-2} for catalyst samples. (h) Comparison of OER activity with representative Ir- or Ru-based catalysts in acidic media.

that the large-scale catalyst exhibited OER activity and stability comparable to those of the originally prepared small-batch catalyst (Fig. S18 in the ESM), thereby demonstrating potential for future large-scale production and practical application of this method.

To systematically investigate the origin of the enhanced OER activity of $Ir_xRu_{1-x}O_2/WO_3$, DFT calculations were performed on two models: a heterostructured $Ir_xRu_{1-x}O_2/WO_3$ and a reference $Ir_xRu_{1-x}O_2$ without the heterointerface (Figs. S19 and S20 in the ESM). Considering that morphology modulation by the WO_3 heterostructure may permit the coexistence of single-site-adsorbate-driven and dual-site-adsorbate-driven pathways, we computed both the adsorbate evolution mechanism (AEM) and the OPM and compared their Gibbs free energy profiles on these two models. The values of Gibbs free energy calculations are presented in Table S5 in the ESM.

In the AEM pathway, the reaction proceeds via sequential proton-coupled electron transfer (PCET) steps *OH → *O → *OOH → O_2 (Fig. 4(a)) [16, 38]. On $Ir_xRu_{1-x}O_2/WO_3$, the potential-determining step (PDS) is *O → *OOH, giving a theoretical overpotential (η) of 1.12 V. By contrast, $Ir_xRu_{1-x}O_2$ without the heterostructure exhibited its PDS at the subsequent *OOH → O_2 step, requiring a significantly higher overpotential of 1.59 V. In comparison, the OPM bypasses the high-energy *OOH intermediate via direct O–O coupling between adjacent surface *O species (Fig. 4(b)) [39, 40]. Under this mechanism, the $Ir_xRu_{1-x}O_2/WO_3$ displayed a PDS at the *OH + *O → *O + *O step, with a much lower overpotential of 0.70 V. Meanwhile, the $Ir_xRu_{1-x}O_2$ showed its PDS at the *O + *O → O_2 coupling step with an overpotential as high as 2.33 V (Fig. 4(c)). These results suggest that the spatial constraints in $Ir_xRu_{1-x}O_2$ limit the accessibility of the OPM, thus enforcing the use of the less favorable AEM. In contrast, the introduction of the WO_3 heterostructure effectively expands the spacing between adjacent metal active sites, rendering the OPM pathway kinetically feasible [41]. This hypothesis is supported by the interatomic distances between adjacent Ru sites at the dual active centers. Structural analysis revealed that the Ru–Ru distance in $Ir_xRu_{1-x}O_2/WO_3$ is increased to 3.18 Å, compared to 3.09 Å in $Ir_xRu_{1-x}O_2$ (Fig. S21 in the ESM), thereby facilitating the dual-site O–O coupling process.

Moreover, Bader charge analysis at the interface further substantiates the presence of electronic redistribution induced by the WO_3 heterostructure. Both Ru and Ir atoms in $Ir_xRu_{1-x}O_2/WO_3$ exhibit lower Bader charges compared to their counterparts in

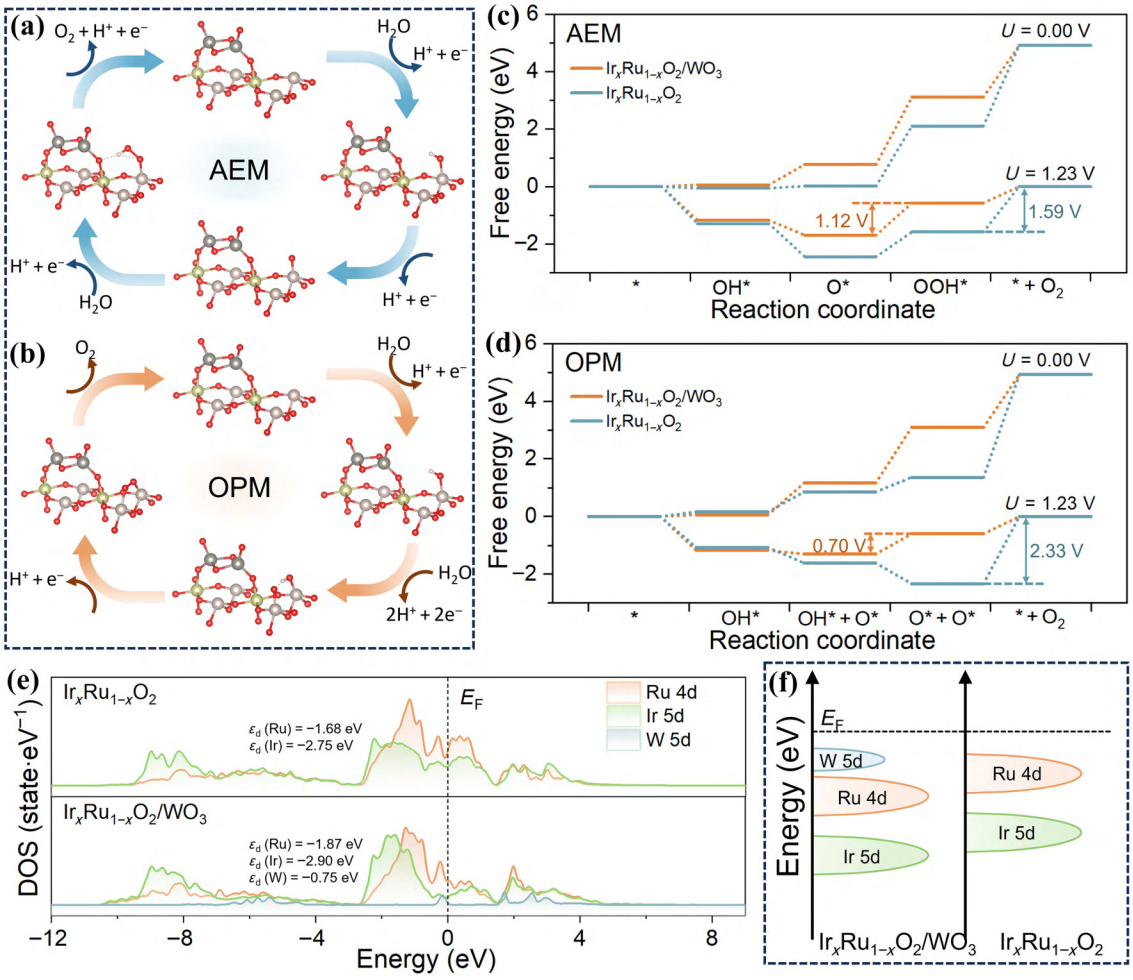

Figure 4 DFT calculations of $Ir_xRu_{1-x}O_2/WO_3$. ((a) and (b)) Schematic illustration of (a) AEM and (b) OPM mechanism on the $Ir_xRu_{1-x}O_2/WO_3$ (green: Ir; light gray: Ru; dark gray: W; red: O; and white: H). ((c) and (d)) Gibbs free energy diagrams of OER steps via (c) AEM and (d) OPM pathway at the potential of 0 and 1.23 V for $Ir_xRu_{1-x}O_2/WO_3$ and $Ir_xRu_{1-x}O_2$. (e) The PDOS curves for $Ir_xRu_{1-x}O_2/WO_3$ and $Ir_xRu_{1-x}O_2$. (f) Schematic diagram of d-band structure for $Ir_xRu_{1-x}O_2/WO_3$ and $Ir_xRu_{1-x}O_2$.

$Ir_xRu_{1-x}O_2$, indicative of enhanced electron delocalization across the interface (Fig. S22 and Table S6 in the ESM). This observation is corroborated by the differential charge density plot of $Ir_xRu_{1-x}O_2/WO_3$ (Fig. S23 in the ESM), which highlights pronounced interfacial charge reorganization. Such an effect is expected to facilitate the initial adsorption of O_2 species during OER catalysis.

To further explore the influence of the heterointerface on the local electronic structure, we analyzed the partial DOS (PDOS) of Ru, Ir, and W d-orbitals (Fig. 4(e)). A marked downshift in the d-band center (ε_d) of both Ru and Ir was observed in $Ir_xRu_{1-x}O_2/WO_3$ relative to $Ir_xRu_{1-x}O_2$, with ε_d shifting from −1.68 and −2.75 eV to −1.87 and −2.90 eV, respectively. This downshift of the d-band center is schematically illustrated in Fig. 4(f). It indicates a weakened interaction between active sites and oxygen intermediates, thereby facilitating intermediate desorption and lowering the energy barrier for the final O_2 release step—previously identified as the PDS in $Ir_xRu_{1-x}O_2$ [42, 43]. Moreover, similar downshifts in ε_d were observed in the PDOS of key OPM intermediates (*O + *O and *OH + *O) on $Ir_xRu_{1-x}O_2/WO_3$ (Fig. S24 in the ESM), further confirming the electronic modulation of the active center. Thus, DFT calculations reveal that the atomic and electronic modulation of the $Ir_xRu_{1-x}O_2/WO_3$ heterointerface enables a more efficient OER via the OPM pathway.

EOG is a PEM-compatible energy conversion approach that we previously developed [44, 45]. Under an applied potential, it drives the directional transport of ambient O_2 from low to high concentrations. During operation, air was introduced into the cathode compartment via a gas pump, where the O_2 component is reduced through the ORR, while OER occurred at the anode, generating O_2 that was subsequently expelled along with the water feed (Fig. 5(a)). The catalytic capability of $Ir_xRu_{1-x}O_2/WO_3$ was evaluated by assembling it into the EOG single cell with an active area of 50 cm^2. As illustrated in Fig. S25 in the ESM, the catalyst-coated membrane (CCM) configuration was employed, with $Ir_xRu_{1-x}O_2/WO_3$ and commercial Pt/C serving as the anodic and cathodic catalysts, respectively. A titanium mesh was used as the anodic current collector, while a gas diffusion electrode (GDE) was applied on the cathode side to ensure efficient mass transport of gaseous reactants. The cell components were assembled using flow plates with serpentine channels, which minimized Ohmic resistance and enabled excellent proton conductivity under liquid-electrolyte-free conditions [46–48]. Photographs of the EOG single cell and its structure with assembled connections are shown in Figs. S26 and S27 in the ESM.

Polarization curves comparing $Ir_xRu_{1-x}O_2/WO_3$ and commercial IrO_2 as anodic catalysts under varying voltages are shown in Fig. 5(b). At an operating voltage of 1.2 V, the $Ir_xRu_{1-x}O_2/WO_3$-

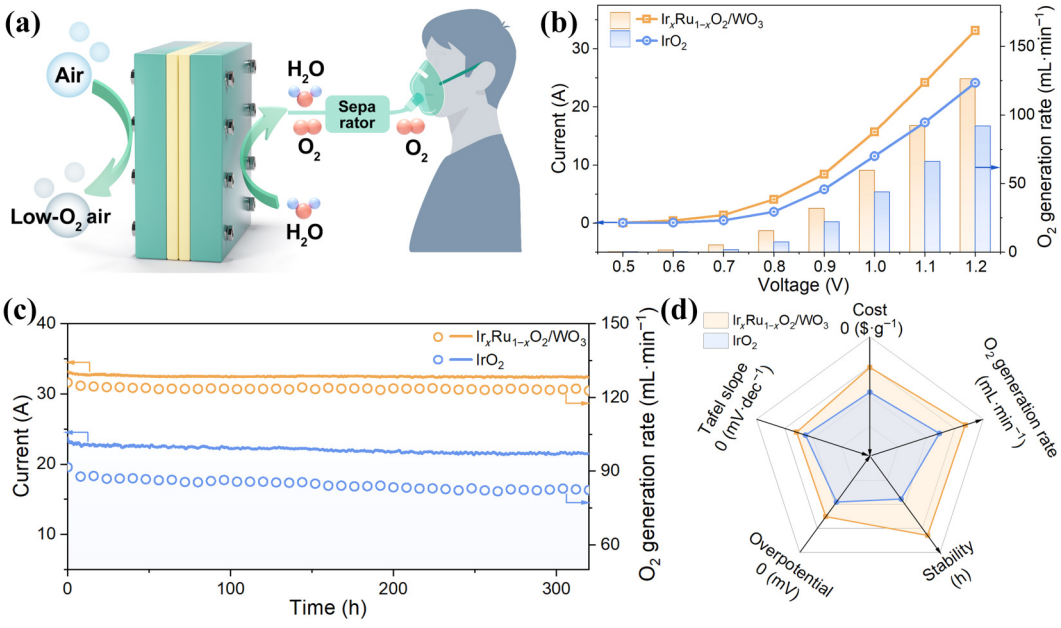

Figure 5 Performance evaluation of $Ir_xRu_{1-x}O_2/WO_3$ in the EOG device. (a) Schematic illustration of the EOG working principle. (b) Polarization curves and corresponding oxygen evolution rates of $Ir_xRu_{1-x}O_2/WO_3$ and IrO_2 in the EOG. (c) Stability comparison of $Ir_xRu_{1-x}O_2/WO_3$ and IrO_2 in the EOG under a constant voltage of 1.2 V. (d) Radar chart of key performance metrics comparison between $Ir_xRu_{1-x}O_2/WO_3$ and IrO_2.

based device delivered a current of 33.2 A and an oxygen production rate of 126 mL·min^{-1}, significantly outperforming the IrO_2 counterpart, which achieved 24.2 A and 92 mL·min^{-1} under the same conditions. Gas chromatography (GC) analysis confirmed that the oxygen produced by $Ir_xRu_{1-x}O_2/WO_3$ possessed a high purity of 99.95% (Fig. S28 and Table S7 in the ESM). Table S8 in the ESM compares the performance of the EOG single cell in this work with that reported in previous studies. As shown, our device achieves highly competitive current densities and oxygen production rates among reported systems, while operating under relatively mild conditions (25 °C, deionized (DI) water). In durability tests conducted at a constant voltage of 1.2 V, the $Ir_xRu_{1-x}O_2/WO_3$-based system exhibited exceptional long-term stability over 320 h, with less than 3% fluctuation in current and oxygen output (Fig. 5(c)). In contrast, the IrO_2-based system showed a pronounced performance degradation of up to 15% under identical conditions. To further verify the catalyst robustness under industrially relevant high-current operation, a stability test at a constant current density of 0.5 A·cm^{-2} was performed. After 300 h of continuous operation, the cell voltage increased by only 31 mV (from 1.109 to 1.140 V). Meanwhile, the current density at 1.2 V decreased by merely 24.4 mA·cm^{-2} (from 663.4 to 639.0 mA·cm^{-2}), evidencing minimal voltage drift and negligible polarization degradation during prolonged high-current operation (Fig. S29 in the ESM).

Subsequently, we quantified the catalyst's compositional evolution after the stability test by inductively coupled plasma (ICP) analysis to determine changes in elemental contents. The results show only minor variations in the overall composition: The Ir content increases slightly, whereas the Ru and W contents decrease marginally, consistent with the relatively higher dissolution tendency of Ru and W during operation (Table S9 in the ESM). In parallel, SEM image comparisons indicate that after 300 h of continuous operation, the sample largely retains its nanosheet morphology, showing only a slightly reduced lateral size and more fragmented edges, which suggests mild surface etching under prolonged high-current-density conditions (Fig. S30 in the ESM). XRD measurements were further used to assess whether long-term operation induces any structural transformation. The results show essentially unchanged peak positions and relative intensities of $Ir_xRu_{1-x}O_2/WO_3$, indicating the absence of pronounced phase transformation or lattice reconstruction during the test (Fig. S31 in the ESM). In addition, XPS results reveal small positive shifts in the binding energies of Ir, Ru, and W after operation, implying a slightly higher average oxidation state of surface metal sites under acidic OER conditions; however, the limited magnitude of these shifts suggests that the overall surface chemical environment remains largely preserved (Fig. S32 in the ESM).

Overall, complementary post-test characterizations indicate that $Ir_xRu_{1-x}O_2/WO_3$ undergoes only minor changes and shows no evident structural degradation during the test, demonstrating robust stability under prolonged high-current acidic OER conditions.

A comprehensive radar chart analysis (Fig. 5(d) and Table S10 in the ESM) comparing key performance metrics—including cost, oxygen production rate, stability, overpotential, and Tafel slope—further highlights the superior performance of $Ir_xRu_{1-x}O_2/WO_3$ relative to commercial IrO_2. These results collectively underscore the strong potential of this heterostructured catalyst for practical deployment in advanced electrochemical oxygen generation technologies.

3 Conclusions

In summary, we achieved the large-scale synthesis of the heterostructured nanosheet catalyst $Ir_xRu_{1-x}O_2/WO_3$ via a molten-salt method. The ultrathin $Ir_xRu_{1-x}O_2/WO_3$ nanosheets deliver a low overpotential of 223 mV at 10 mA·cm^{-2} and maintain an essentially constant potential over 120 h during chronopotentiometry. DFT calculations attribute the performance enhancement to WO_3-driven modulation of active-site geometry and electronic states, suggesting that an OPM contribution helps lower the OER energy barrier.

When integrated into a PEM-EOG single cell, the catalyst sustains high throughput—664 mA·cm^{-2} at 1.2 V and 126 mL·min^{-1} O_2 per cell. The single cell also exhibits excellent stability, with less than 3% current decay over 320 h of continuous operation. These results highlight WO_3-mediated interfacial engineering as a promising strategy for high-performance acidic OER anodes and advance the practical deployment of PEM-EOG technology.

Electronic Supplementary Material: Supplementary material (experimental procedures, detailed TEM and SEM images, XRD patterns, XPS spectra, electrochemical test results, catalyst structural models, photograph and schematic illustration of EOG, and tables) is available in the online version of this article at https://doi.org/10.26599/NR.2026.94908622.

Data availability

All data needed to support the conclusions in the paper are presented in the manuscript and the Electronic Supplementary Material. Additional data related to this paper may be requested from the corresponding author upon request.

Acknowledgements

This work was supported by China Ministry of Science and Technology (No. 2020YFA0710203), the National Natural Science Foundation of China (Nos. 92261105, 22221003, 22425302, and 22505244), the Joint Funds of the National Natural Science Foundation of China (No. U23A2081), the Original Exploratory Program Project of the National Natural Science Foundation of China (No. 22550001), the Anhui Provincial Natural Science Foundation (Nos. 2208085UD04, 2108085UD06, and 2408085MB031), the Key Technologies R&D Program of Anhui Province (Nos. 2023z04020010 and 2022a05020053), the Joint Funds from Hefei National Synchrotron Radiation Laboratory (No. KY2060000180), the Fundamental Research Funds for the Centre Universities (No. WK9990000155), the Joint Funds from Hefei National Synchrotron Radiation Laboratory (No. KY2060000195), and USTC Research Funds of the Double First-Class Initiative (No. YD2060002029). This work was partially carried out at the USTC Center for Micro and Nanoscale Research and Fabrication. We acknowledge the Experimental Center of Engineering and Material Science in the University of Science and Technology of China.

Declaration of competing interest

All the contributing authors report no conflict of interests in this work.

Author contribution statement

Y. T.: Data curation, validation, writing manuscript, experimental design. Y. M. L.: Data curation, investigation, validation. Y. H. W.: Formal analysis, writing manuscript. X. Y. Z.: Experimental design, investigation. D. M. L.: Investigation, validation. S. G.: Resources. Y. F. L.: Funding acquisition, resources. Y. Z.: Project administration. Y. E. W.: Funding acquisition, resources, supervision. All the authors have approved the final manuscript.

Use of AI statement

None.

References

[1] Xu, J.; Yang, Y. T.; Jin, H. Y.; Zheng, Y.; Qiao, S. Z. Bridging gaps between lab- and fab-oriented anode design for proton exchange membrane water electrolyzers. *Chem* **2025**, *11*, 102305.

[2] Carmo, M.; Fritz, D. L.; Mergel, J.; Stolten, D. A comprehensive review on PEM water electrolysis. *Int. J. Hydrogen Energy* **2013**, *38*, 4901–4934.

[3] Liu, R. T.; Xu, Z. L.; Li, F. M.; Chen, F. Y.; Yu, J. Y.; Yan, Y.; Chen, Y.; Xia, B. Y. Recent advances in proton exchange membrane water electrolysis. *Chem. Soc. Rev.* **2023**, *52*, 5652–5683.

[4] Grimaud, A.; Demortière, A.; Saubanère, M.; Dachraoui, W.; Duchamp, M.; Doublet, M. L.; Tarascon, J. M. Activation of surface oxygen sites on an iridium-based model catalyst for the oxygen evolution reaction. *Nat. Energy* **2016**, *2*, 16189.

[5] Fan, Z. L.; Ji, Y. J.; Shao, Q.; Geng, S. Z.; Zhu, W. X.; Liu, Y.; Liao, F.; Hu, Z. W.; Chang, Y. C.; Pao, C. W. et al. Extraordinary acidic oxygen evolution on new phase 3R-iridium oxide. *Joule* **2021**, *5*, 3221–3234.

[6] Liao, F.; Yin, K.; Ji, Y. J.; Zhu, W. X.; Fan, Z. L.; Li, Y. Y.; Zhong, J.; Shao, M. W.; Kang, Z. H.; Shao, Q. Iridium oxide nanoribbons with metastable monoclinic phase for highly efficient electrocatalytic oxygen evolution. *Nat. Commun.* **2023**, *14*, 1248.

[7] Li, L. G.; Wang, P. T.; Shao, Q.; Huang, X. Q. Recent progress in advanced electrocatalyst design for acidic oxygen evolution reaction. *Adv. Mater.* **2021**, *33*, 2004243.

[8] Li, Y. P.; Wang, W. T.; Cheng, M. Y.; Feng, Y. F.; Han, X.; Qian, Q. Z.; Zhu, Y.; Zhang, G. Q. Arming Ru with oxygen-vacancy-enriched RuO_2 sub-nanometer skin activates superior bifunctionality for pH-universal overall water splitting. *Adv. Mater.* **2023**, *35*, 2206351.

[9] Lin, Y. C.; Dong, Y.; Wang, X. Z.; Chen, L. Electrocatalysts for the oxygen evolution reaction in acidic media. *Adv. Mater.* **2023**, *35*, 2210565.

[10] Chen, G. Z.; Lu, R. H.; Ma, C.; Zhang, X. W.; Wang, Z. Y.; Xiong, Y.; Han, Y. H. A long-range disordered RuO_2 catalyst for highly efficient acidic oxygen evolution electrocatalysis. *Angew. Chem., Int. Ed.* **2024**, *63*, e202411603.

[11] Kötz, R.; Stucki, S.; Scherson, D.; Kolb, D. M. *In-situ* identification of RuO_4 as the corrosion product during oxygen evolution on ruthenium in acid media. *J. Electroanal. Chem. Interfacial Electrochem.* **1984**, *172*, 211–219.

[12] Wen, Y. Z.; Chen, P. N.; Wang, L.; Li, S. Y.; Wang, Z. Y.; Abed, J.; Mao, X. N.; Min, Y. M.; Dinh, C. T.; Luna, P. D. et al. Stabilizing highly active Ru sites by suppressing lattice oxygen participation in acidic water oxidation. *J. Am. Chem. Soc.* **2021**, *143*, 6482–6490.

[13] Li, L. M.; Cheng, Z. F.; Su, J. Q.; Song, B. B.; Yu, H.; Ji, Y. J.; Shao, Q.; Lu, J. M. One-dimensional amorphous porous iridium-ruthenium oxide for efficient acidic oxygen evolution reaction. *J. Mater. Chem. A* **2023**, *11*, 25268–25274.

[14] Zhu, W. X.; Song, X. C.; Liao, F.; Huang, H.; Shao, Q.; Feng, K.; Zhou, Y. J.; Ma, M. J.; Wu, J.; Yang, H. et al. Stable and oxidative charged Ru enhance the acidic oxygen evolution reaction activity in two-dimensional ruthenium-iridium oxide. *Nat. Commun.* **2023**, *14*, 5365.

[15] Zi, Y. H.; Zhang, C. X.; Zhao, J. Q.; Cheng, Y.; Yuan, J. L.; Hu, J. Research progress in structure evolution and durability modulation of Ir- and Ru-based OER catalysts under acidic conditions. *Small* **2024**, *20*, 2406657.

[16] He, J.; Zhou, X.; Xu, P.; Sun, J. M. Regulating electron redistribution of intermetallic iridium oxide by incorporating Ru for efficient acidic water oxidation. *Adv. Energy Mater.* **2021**, *11*, 2102883.

[17] Jia, R. L.; Tan, Y.; Li, A. S.; Wang, Y. J.; Cheng, C. W. 3D ordered RuO_2/WO_3 heterostructure inverse opal arrays for highly-active and stable acidic oxygen evolution reaction. *Nano Res. Energy* **2025**, *4*, e9120141.

[18] Song, H. Q.; Yong, X.; Waterhouse, G. I. N.; Yu, J. K.; Wang, H.;

Cai, J. M.; Tang, Z. Y.; Yang, B.; Chang, J. W.; Lu, S. Y. RuO_2–CeO_2 lattice matching strategy enables robust water oxidation electrocatalysis in acidic media via two distinct oxygen evolution mechanisms. *ACS Catal.* **2024**, *14*, 3298–3307.

[19] Jia, W. Q.; Cao, X. J.; Chen, X. J.; Qin, H. Y.; Miao, L. C.; Wang, Q. L.; Jiao, L. F. γ-MnO_2 as an electron reservoir for RuO_2 oxygen evolution catalyst in acidic media. *Small* **2024**, *20*, 2310464.

[20] Li, Y.; Hassan, M. S.; Zhao, X.; Rogach, A. L. Heterostructured electrocatalysts: From fundamental microkinetic model to electron configuration and interfacial reactive microenvironment. *Adv. Mater.* **2025**, *37*, 2418146.

[21] Zhou, Y. T.; Liu, Y. F.; Tang, H. H.; Lin, B. L. The RuO_2/NiRu heterogeneous interface optimizes the d-band center of the Ni–Ru catalyst for high-performance alkaline hydrogen evolution reaction. *J. Mater. Chem. A* **2023**, *11*, 10720–10726.

[22] Wang, Z. Z.; Shen, S. J.; Wang, J. C.; Zhong, W. W. Modulating the D-band center of electrocatalysts for enhanced water splitting. *Chem.—Eur. J.* **2024**, *30*, e202402725.

[23] Jiao, S. L.; Fu, X. W.; Huang, H. W. Descriptors for the evaluation of electrocatalytic reactions: d-band theory and beyond. *Adv. Funct. Mater.* **2022**, *32*, 2107651.

[24] Song, W. Q.; Zhang, R.; Bai, X.; Jia, Q. Q.; Ji, H. M. Exposed crystal facets of WO_3 nanosheets by phase control on NO_2-sensing performance. *J. Mater. Sci.: Mater. Electron.* **2020**, *31*, 610–620.

[25] Lee, S. H.; Cheong, H. M.; Liu, P.; Smith, D.; Tracy, C. E.; Mascarenhas, A.; Roland Pitts, J.; Deb, S. K. Raman spectroscopic studies of gasochromic a-WO_3 thin films. *Electrochim. Acta* **2001**, *46*, 1995–1999.

[26] Warmer, J.; Breuch, R.; Schöning, M. J.; Wagner, P.; Kaul, P. Temperature-dependent *operando* Raman analysis of a WO_3-based metal-oxide gas sensor detecting triacetone triperoxide. *Phys. Status Solidi (A)* **2024**, *221*, 2300790.

[27] Devadas, A.; Baranton, S.; Coutanceau, C. Green synthesis and modification of RuO_2 materials for the oxygen evolution reaction. *Front. Energy Res.* **2020**, *8*, 571704.

[28] Korotcov, A.; Hsu, H. P.; Huang, Y. S.; Tsai, D. S. Raman scattering characterization of well-aligned IrO_2 nanocrystals grown on sapphire substrates via reactive sputtering. *J. Raman Spectrosc.* **2006**, *37*, 1411–1415.

[29] Niu, Z. Q.; Lu, Z. K.; Qiao, Z. L.; Wang, S. T.; Cao, X. H.; Chen, X. D.; Yun, J.; Zheng, L. R.; Cao, D. P. Robust Ru–VO_2 bifunctional catalysts for all-pH overall water splitting. *Adv. Mater.* **2024**, *36*, 2310690.

[30] Wang, Y.; Yang, R.; Ding, Y. J.; Zhang, B.; Li, H.; Bai, B.; Li, M. R.; Cui, Y.; Xiao, J. P.; Wu, Z. S. Unraveling oxygen vacancy site mechanism of Rh-doped RuO_2 catalyst for long-lasting acidic water oxidation. *Nat. Commun.* **2023**, *14*, 1412.

[31] Deng, L. M.; Hung, S. F.; Lin, Z. Y.; Zhang, Y.; Zhang, C. C.; Hao, Y. X.; Liu, S. Y.; Kuo, C. H.; Chen, H. Y.; Peng, J. et al. Valence oscillation of Ru active sites for efficient and robust acidic water oxidation. *Adv. Mater.* **2023**, *35*, 2305939.

[32] Gao, Y. H.; Song, T.; Guo, X. L.; Zhang, Y.; Yang, Y. Electronic interaction and oxygen vacancy engineering of g-C_3N_4/α-Bi_2O_3 Z-scheme heterojunction for enhanced photocatalytic aerobic oxidative homo-/hetero-coupling of amines to imines in aqueous phase. *Green Carbon* **2023**, *1*, 105–117.

[33] Wei, Z.; Zhao, M. F.; Yang, Z. W.; Duan, X. X.; Jiang, G. X.; Li, G. G.; Zhang, F. L.; Hao, Z. P. Oxygen vacancy-engineered titanium-based perovskite for boosting H_2O activation and lower-temperature hydrolysis of organic sulfur. *Proc. Natl. Acad. Sci.* **2023**, *120*, e2217148120.

[34] Sun, Y. H.; Xiao, M. Y.; Liu, F.; Gan, J.; Gao, S. X.; Liu, J. J. Oxygen vacancy-electron polarons featured $InSnRuO_2$ oxides: Orderly and concerted In–Ov–Ru–O–Sn substructures for acidic water oxidation. *Adv. Mater.* **2024**, *36*, 2414579.

[35] van der Merwe, M.; Lee, Y.; Wibowo, R. E.; Kokumai, T.; Efimenko, A.; Arce, M. D.; Jimenez, C. E.; Howchen, B.; Suarez Anzorena, R.; Lucentini, I. et al. Unravelling the mechanistic complexity of the oxygen evolution reaction and Ir dissolution in highly dimensional amorphous hydrous iridium oxides. *Energy Environ. Sci.* **2025**, *18*, 1214–1231.

[36] He, J. Y.; Chen, W. X.; Gao, H. M.; Chen, Y. X.; Zhou, L.; Zou, Y. Q.; Chen, R.; Tao, L.; Lu, X.; Wang, S. Y. Tuning hydrogen binding modes within RuO_2 lattice by proton and electron co-doping for active and stable acidic oxygen evolution. *Chem. Catal.* **2022**, *2*, 578–594.

[37] Chen, J. D.; Chen, C. H.; Qin, M. K.; Li, B.; Lin, B. B.; Mao, Q.; Yang, H. B.; Liu, B.; Wang, Y. Reversible hydrogen spillover in Ru–WO_{3-x} enhances hydrogen evolution activity in neutral pH water splitting. *Nat. Commun.* **2022**, *13*, 5382.

[38] Cui, X. J.; Ren, P. J.; Ma, C.; Zhao, J.; Chen, R. X.; Chen, S. M.; Rajan, N. P.; Li, H. B.; Yu, L.; Tian, Z. Q. et al. Robust interface Ru centers for high-performance acidic oxygen evolution. *Adv. Mater.* **2020**, *32*, 1908126.

[39] Wang, C. K.; Wu, X. R.; Sun, H.; Xu, Z.; Xu, C.; Wang, X.; Li, M.; Wang, Y.; Tang, Y. W.; Jiang, J. C. et al. An asymmetric RE–O–Ru unit with bridged oxygen vacancies accelerates deprotonation during acidic water oxidation. *Energy Environ. Sci.* **2025**, *18*, 4276–4287.

[40] Li, Z. Y.; Wang, D.; Kang, H. G.; Shi, Z. N.; Hu, X. W.; Sun, H. B.; Xu, J. L. Atomic cation and anion co-vacancy defects boosted the oxide path mechanism of the oxygen evolution reaction on NiFeAl-layered double hydroxide. *J. Mater. Chem. A* **2025**, *13*, 587–594.

[41] Qian, F. R.; Cao, D. F.; Chen, S. M.; Yuan, Y. L.; Chen, K.; Chimtali, P. J.; Liu, H. J.; Jiang, W.; Sheng, B. B.; Yi, L. C. et al. High-entropy RuO_2 catalyst with dual-site oxide path for durable acidic oxygen evolution reaction. *Nat. Commun.* **2025**, *16*, 6894.

[42] Cao, X. J.; Miao, L. C.; Jia, W. Q.; Qin, H. Y.; Lin, G. L.; Ma, R. P.; Jin, T.; Jiao, L. F. Strain heterogeneity in RuO_2 for efficient acidic oxygen evolution reaction in proton exchange membrane water electrolysis. *Nat. Commun.* **2025**, *16*, 6217.

[43] Qin, R.; Chen, G. Z.; Feng, X. T.; Weng, J. N.; Han, Y. H. Ru/Ir-based electrocatalysts for oxygen evolution reaction in acidic conditions: From mechanisms, optimizations to challenges. *Adv. Sci.* **2024**, *11*, 2309364.

[44] Zhao, X. Y.; Zhao, J.; Li, D. M.; Zhou, F. Y.; Li, P.; Tan, Y.; Zhou, H.; Zhang, Y.; Lin, S.; Wu, Y. E. Electrolyte-free electrochemical oxygen generator for providing sterile and medical-grade oxygen in household applications. *Device* **2024**, *2*, 100360.

[45] Zhang, Y.; Xie, K.; Zhou, F. Y.; Wang, F. T.; Xu, Q.; Hu, J.; Ding, H. H.; Li, P.; Tan, Y.; Li, D. M. et al. Electrochemical oxygen generator with 99.9% oxygen purity and high energy efficiency. *Adv. Energy Mater.* **2022**, *12*, 2201027.

[46] Chen, F. Y.; Wu, Z. Y.; Adler, Z.; Wang, H. T. Stability challenges of electrocatalytic oxygen evolution reaction: From mechanistic understanding to reactor design. *Joule* **2021**, *5*, 1704–1731.

[47] Liang, H. G.; Su, H. N.; Pollet, B. G.; Pasupathi, S. Development of membrane electrode assembly for high temperature proton exchange membrane fuel cell by catalyst coating membrane method. *J. Power Sources* **2015**, *288*, 121–127.

[48] Yu, L.; Tian, B.; Huang, W. T.; Zhou, X. C.; Li, W. H. Advancements in ordered membrane electrode assembly (MEA) for water electrolysis. *Curr. Opin. Electrochem.* **2024**, *48*, 101595.